JOURNAL OF GUIDANCE, CONTROL, AND DYNAMICS
Vol. 24, No. 3, May–June 2001

Influence of Unstable Manifolds on Orbit Uncertainty

D. J. Scheeres*
University of Michigan, Ann Arbor, Michigan 48109-2140
D. Han†
Jet Propulsion Laboratory, California Institute of Technology, Pasadena, California 91109-8099
and
Y. Hou‡
Iowa State University, Ames, Iowa 50011-3231

The dynamics of orbit uncertainty in an unstable orbital environment are discussed with specific application to the orbit determination of a halo orbit about an Earth–sun libration point. The goal of the paper is to investigate orbit determination and orbit uncertainty dynamics in this environment and to present basic results. The dynamics model is based on the Hill equations of motion, and the orbit determination measurement model is based on the classical Hamilton–Melbourne analysis for the information content of a Doppler pass of data. The effect of correlated stochastic accelerations on the orbit uncertainty distributions is also included in the model. Results are presented, and the major departures from the classic two-body orbital environment are highlighted. We show that the unstable manifolds of the halo orbit control the long-term evolution of the uncertainty. During active periods of tracking, however, this relationship can be reversed, and the largest direction of uncertainty will not, in general, lie along the local unstable manifold of the orbit. The influence of the unstable manifold on the direction of maximum orbit uncertainty is seen to vary with the orbit geometry, level of stochastic accelerations, and tracking frequency.

I. Introduction

THE dynamics of orbit determination uncertainties are studied for a spacecraft in an unstable halo orbit in the Earth–sun system. To bring the essential nature of the dynamics into clear focus, we use simple, yet qualitatively accurate, models for the spacecraft dynamics and for the orbit determination measurements. The orbit trajectory is analyzed using the Hill problem, which has a very simple specification, yet contains all of the essential difficulties of the more general restricted three-body problem.[1] The measurement information content is modeled using the classic Hamilton–Melbourne analysis,[2] modified so that it can be used in a square-root information filter formulation. Finally, for realism, our model includes process noise in the form of stochastic accelerations that modify the dynamics of the orbit uncertainty. This study does not address the nonlinear effects that an unstable manifold will have on the orbit uncertainty distribution but leaves this for future investigations (cf. Junkins et al.[3] for an introduction to this problem for near-Keplerian orbits).

The current paper is intended to investigate the basic processes at work in the orbit determination of a spacecraft in a highly unstable libration point halo orbit.[4] This is a fundamentally different orbital environment from that found for planetary or solar orbiters as evidenced by recent results concerning the design and implementation of the Genesis mission,[5] where extremely sensitive trajectories must be flown in an environment where there are great pressures to decrease the total tracking time of spacecraft (in order to decrease overall costs). Given an improved understanding of orbit determination in this environment, it becomes possible to understand the impact of reduced tracking on uncertainty distributions and may eventually lead to the identification of "optimal" times to track the spacecraft—potentially leading to reduced tracking times during other periods.

Presented as Paper 98-4559 at the AIAA/AAS Astrodynamics Specialist Conference, Boston, MA, 10–12 August 1998; received 11 November 1999; revision received 1 September 2000; accepted for publication 25 September 2000.

*Assistant Professor, Department of Aerospace Engineering; scheeres@umich.edu. Senior Member AIAA.
†Senior Engineer, Navigation and Flight Mechanics Section, 4800 Oak Grove Drive.
‡Graduate Student, Department of Aerospace Engineering and Engineering Mechanics.

II. Model Definition

A. Force Model and Trajectory

This paper models a spacecraft trajectory that mimics the Genesis Halo orbit, a highly unstable, non-Keplerian trajectory.[5] To define the trajectory, we use an approximation to the three-body problem, known as Hill's problem,[1] to model the spacecraft motion. This approximate model is simple to state yet fully captures the relevant dynamics of the three-body problem for motion close to the second, smaller primary (Earth in this case). There are three basic assumptions needed to derive this model,[6] all satisfied for the Earth–sun system: that the spacecraft is relatively close to the Earth, that the mass of the Earth is much smaller than that of the sun, that the Earth lies on a near-circular orbit about the sun. Making these assumptions leads to the equations of motion, specified in the frame centered at the Earth and rotating with the Earth–sun line:

$$\ddot{x} - 2\omega\dot{y} = \frac{\partial V}{\partial x}, \qquad \ddot{y} + 2\omega\dot{x} = \frac{\partial V}{\partial y} \tag{1}$$

$$\ddot{z} = \frac{\partial V}{\partial z}, \qquad V = \frac{\mu}{r} + \frac{3}{2}\omega^2 x^2 - \frac{1}{2}\omega^2 z^2 \tag{2}$$

where $r = \sqrt{(x^2 + y^2 + z^2)}$, ω is the Earth's rotation frequency about the sun (corresponding to a period of one year) and is the rotation rate of the coordinate frame, and μ is the mass parameter of the Earth. In this rotating frame the x axis points away from the sun, and the z axis points normal to the Earth's orbital plane, with the y axis completing the triad. These equations of motion contain analogues to the L1 and L2 points in the three-body problem and can recreate all of the qualitative dynamical phenomenon about these points.[7]

Equations (1) have been numerically integrated to find a periodic halo orbit with similar characteristics to the Genesis halo orbit. The orbit has a period of just under 179 days and is plotted (in the coordinate frame rotating with the sun–Earth line) in Figs. 1–3. This is an unstable periodic orbit with a single hyperbolic instability. The Lyapunov characteristic exponent (LCE) of the orbit corresponding to the hyperbolic instability is 4.756×10^{-7}/s or 0.041/day, corresponding to an expansion of 1.562×10^3 over one orbit period. Corresponding to the hyperbolic unstable term is a hyperbolic stable term with an LCE equal and negative to the unstable LCE,

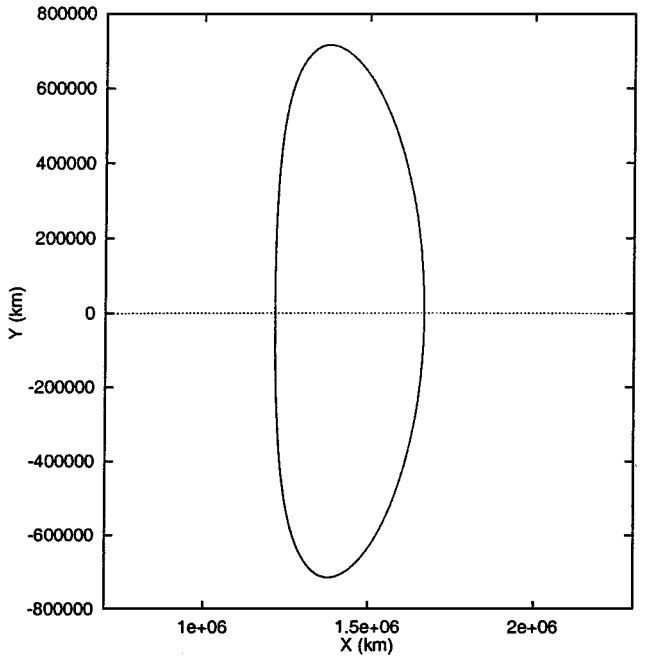

Fig. 1 *X–Y* **projection of halo orbit. The sun and the Earth lie along the** $-X$ **direction. Motion occurs in the counterclockwise direction.**

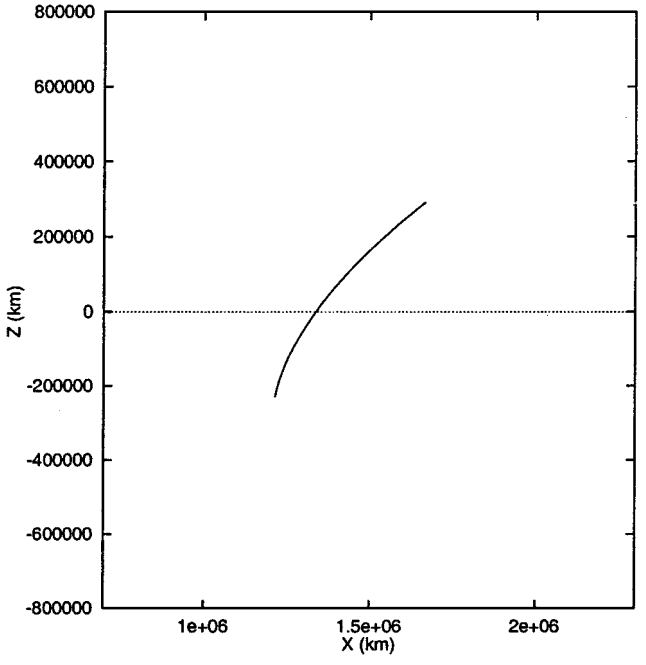

Fig. 2 *X–Z* **projection of halo orbit. The sun and the Earth lie along the** $-X$ **direction. Because of symmetries in the model, the periodic motion projects onto a line in this coordinate plane.**

corresponding to a contraction of 6.4×10^{-4} over one orbit period. The remaining terms consist of a two-dimensional center manifold with an oscillation period slightly greater than the orbit period, plus the usual two unity eigenvalues for a closed periodic orbit corresponding to displacements along the orbit and along the surface of constant Jacobi energy.[8]

B. Trajectory Stability Characterization

For the analysis performed here, it is the stability properties of the trajectory over times less than one orbit period that are important. For the orbit determination process we are interested in the orbital dynamics between measurement updates, which occur every few days to weeks. To accomodate this, a generalization of the concept of stable and unstable orbits must be made that applies to

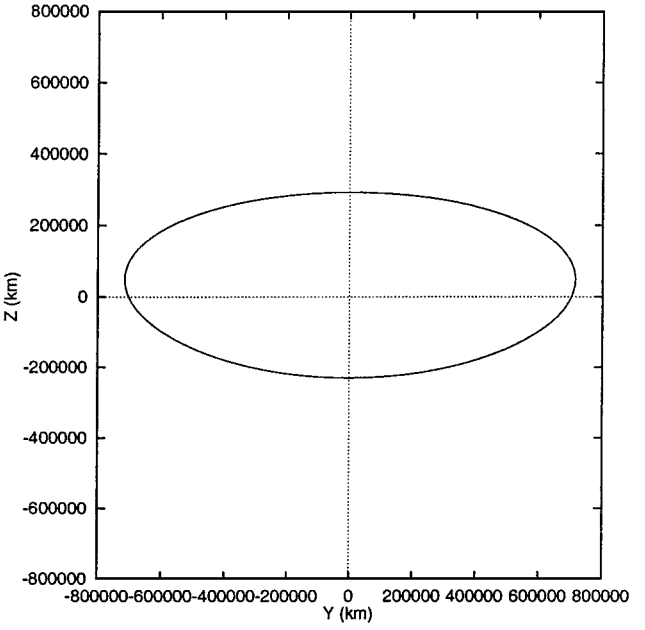

Fig. 3 *Y–Z* **projection of halo orbit. Motion occurs in the counterclockwise direction.**

relatively short periods of time—what we call the *local stability characteristics of the orbit.*

These characteristics can be defined using the state transition matrix (STM) evaluated along the trajectory. The STM, $\Phi(t, t_0)$, is computed by integrating the variational equations simultaneously with the trajectory equations:

$$\dot{\Phi}(t, t_0) = A\Phi(t, t_0) \tag{3}$$

$$\Phi(t_0, t_0) = I_{6\times 6} \tag{4}$$

$$A = \begin{bmatrix} 0_{3\times 3} & I_{3\times 3} \\ V_{rr} & 2\omega J \end{bmatrix} \tag{5}$$

$$J = \begin{bmatrix} 0 & 1 & 0 \\ -1 & 0 & 0 \\ 0 & 0 & 0 \end{bmatrix} \tag{6}$$

where V_{rr} is the second partial of the force potential V with respect to the spacecraft position vector. The matrix A will vary with the position of the spacecraft in its halo orbit. Thus, the STM is implicitly a function of the current and initial time as well as the initial state, or $\Phi(t, t_0; \boldsymbol{r}_0, \boldsymbol{v}_0)$. Thus, when the computation of the STM is initialized at different locations along the orbit its local characteristics are expected to change. It is only when the STM is computed over one (or multiple) orbit periods that it is equal to the monodromy map,[8] and the stability characteristics become independent of initial time and state, according to Floquet Theory.[9]

Now consider the general situation when the STM maps between two times within the nominal periodic orbit $\Phi(t, t_0; \boldsymbol{r}_0, \boldsymbol{v}_0)$, where $t - t_0$ is less than one orbit period. The eigenvalues and eigenvectors of Φ can be computed at each moment of time and are designated as $(\lambda_i, \boldsymbol{e}_i, \boldsymbol{f}_i)$, $i = 1, 2, \ldots, 6$, where the λ_i are the eigenvalues of Φ, the $\boldsymbol{e}_i$ are the corresponding right eigenvectors of Φ, and $\boldsymbol{f}_i$ are the corresponding left eigenvectors of Φ. The state transition matrix can then be expressed as[10]

$$\Phi = \sum_{i=1}^{6} \lambda_i \boldsymbol{e}_i \boldsymbol{f}_i^T \tag{7}$$

The eigenvalues λ_i follow the same basic rules as are found for periodic orbits,[8] where if λ_i is an eigenvalue then so are $\bar{\lambda}_i$, λ_i^{-1}, and $\bar{\lambda}_i^{-1}$, where the overbar denotes complex conjugation.

For a given Φ we consider an eigenvalue with $|\lambda_i| > 1$ to be unstable and its corresponding right eigenvector $\boldsymbol{e}_i$ to define its local

"unstable manifold," that is, the direction relative to the nominal trajectory in which the instability acts. An eigenvalue with $|\lambda_i| < 1$ is considered to be stable, and its corresponding right eigenvector $\boldsymbol{e}_i$ defines its local stable manifold. Finally, the eigenvalues with $|\lambda_i| = 1$ are oscillatory, and their eigenvectors define the center manifold. Whereas the STM computed over one period about a periodic orbit in a time-invariant system will always have two eigenvalues equal to 1, a STM computed over a time span noncommensurate with the orbital period will, in general, not have any eigenvalues equal to unity. Rather, the unity eigenvalues for the monodromy map will in general lie on the unit circle, but off of the real axis, when evaluated over less than one period.

As just defined, the local manifolds $\boldsymbol{e}_i$ and characteristics λ_i of the orbit are a function of time and initial state on the periodic orbit. As the time is varied for a given initial state, the spectrum of the STM can suffer bifurcations, similar to the possible changes in the stability of a periodic orbit as the problem parameters are varied.[8] As an example we show the eigenvalues of our periodic orbit as a function of time in Fig. 4. To "normalize" our presentation of eigenvalues, the plot shows the finite time LCEs,[11] defined as

$$\mathrm{LCE}_i = \frac{\ell n|\lambda(t, t_0)_i|}{t - t_0} \tag{8}$$

where $|\lambda(t, t_0)_i|$ is the magnitude of the ith eigenvalue of the STM at time t and $t - t_0$ is the length of time from the start of the STM mapping to the current time. The hyperbolic roots (those with strongly positive and negative LCE values) remain defined as a function of time, but the oscillatory roots (those with zero LCE values) experience short intervals in time when they bifurcate into hyperbolic and complex roots and back to oscillatory roots. As expected, the LCEs approach the computed stability characteristics of the periodic orbit as time increases, and if evaluated after multiples of the orbit period ($\sim$179 days) we find that the LCEs are equal to the periodic orbit's characteristics as computed from the monodromy map. The particular form of the spectrum shown in Fig. 4 is peculiar to our specific periodic orbit. If a significantly different periodic or nonperiodic orbit were evaluated, the resulting LCEs could have a significantly different time signature.

Figure 4 corresponds to the pure mapping of an orbit forward in time but does not represent the situation once measurements are incorporated into the dynamical system. In this case the orbit uncertainty distribution becomes updated after every measurement, and the STM must be remapped, starting from the identity matrix. To give an example of how such updates modify the trajectory characteristics, we plot the dominant unstable hyperbolic LCE of the orbit with periodic resets of the STM back to the identity matrix. This corresponds to the orbit covariance being renormalized after every measurement opportunity and the distribution of orbit uncertainty being updated. In the presence of these updates, we see a clear pattern emerge for the variation of the LCEs as a function of time, shown in Fig. 5. Thus we see that the properties of the unstable manifold, as they pertain to the mapping of the orbit uncertainty, will change as a function of frequency of measurement. As the updates to the STM become near continuous, the LCE's approach the spectrum of the A matrix in Eq. (5) evaluated along the periodic orbit.[12]

C. Filter Model

For accuracy purposes the orbit uncertainties are computed and mapped using the square-root information filter (SRIF) formulation.[13] To define the SRIF matrix, first recall the relation between the orbit covariance and information matrix (c.f. Battin[14]):

$$P(t, t_0) = \Lambda(t, t_0)^{-1} \tag{9}$$

where P is the orbit covariance matrix and Λ is the orbit information matrix. The SRIF matrix is then found by computing the square root of the information matrix, defined via

$$\Lambda = R^T R \tag{10}$$

where R is defined as the SRIF matrix. To propagate the orbit uncertainty (or information), we instead propagate the SRIF matrix R because of its improved numerical properties. In the absence of measurements and stochastic accelerations, the SRIF matrix is the adjoint to the STM matrix and maps as

$$R(t, t_0) = R(t_0)\Phi(t_0, t) \tag{11}$$

The presence of stochastic accelerations destroys this ideal property, and the SRIF matrix becomes governed by the following differential equation[15]:

$$\dot{R} = -RA - \tfrac{1}{2} RBP_\omega B^T R^T R \tag{12}$$

where A is the same matrix as defined in Eq. (5) for the variational equations (the partial of the nonlinear state dynamics with respect to the current state), P_ω represents the covariance of the process noise (i.e., random acceleration inputs) and is assumed to be constant, and B maps this noise into the dynamics.

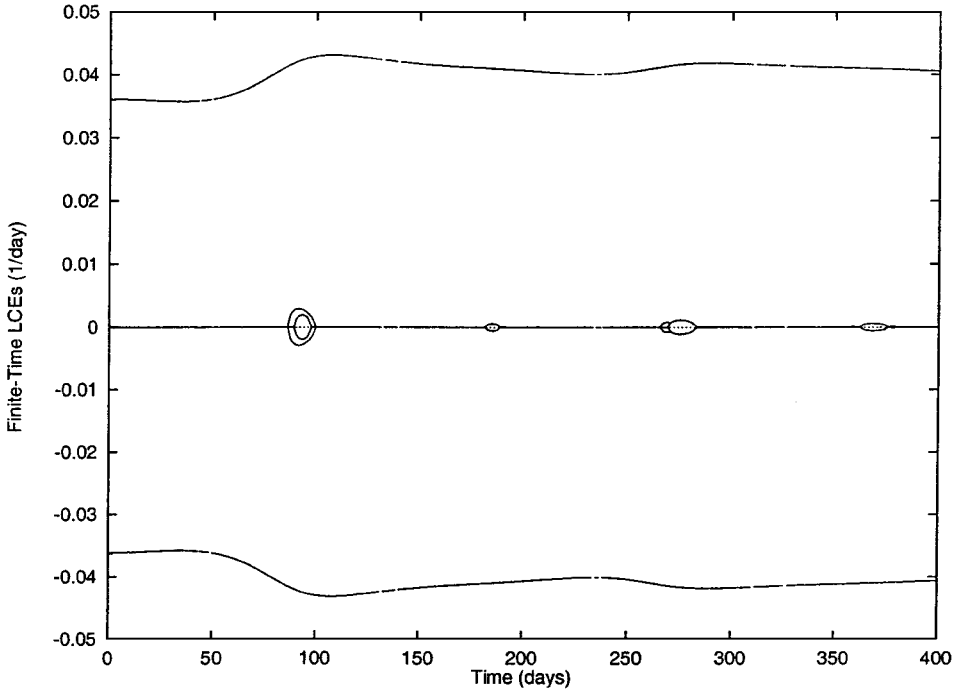

Fig. 4 Finite time Lyapunov characteristic exponents for a mapped STM along the periodic orbit as a function of time. Note the dominant stable and unstable LCEs and that the center manifold LCEs become hyperbolic and complex over limited intervals of time.

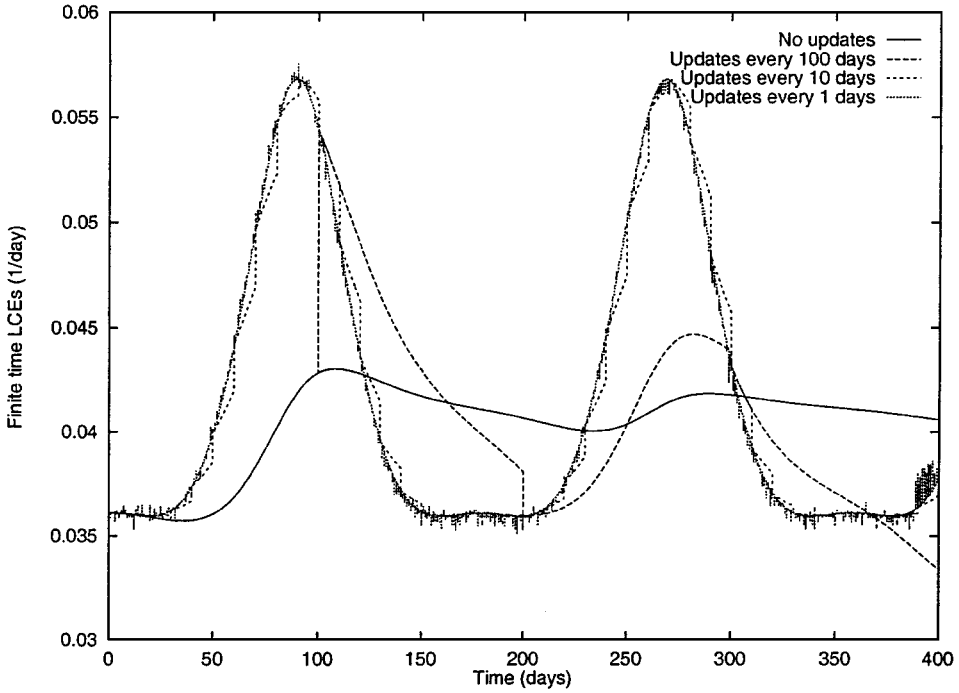

Fig. 5 Maximum finite time Lyapunov characteristic exponents for mapped STMs updated at different frequencies. This shows that the character of the local unstable manifold will change as a function of orbit geometry and tracking.

In the current model the stochastic accelerations are treated as having a constant steady-state uncertainty, implying that they are not being estimated by the orbit determination filter. Under this assumption the matrix B maps P_ω only into the velocity space of the SRIF matrix, and the covariance matrix P_ω has the form

$$P_\omega = 2\tau\sigma_a^2 I_{3\times 3} \tag{13}$$

where τ is the correlation time of the stochastic accelerations and σ_a is the steady-state uncertainty of the acceleration.

Given these definitions, it is possible to directly integrate the orbit uncertainty dynamics in time as the orbit trajectory and state transition matrix are integrated forward in time. The steady-state stochastic acceleration and its correlation time are now parameter inputs to our dynamical system.

D. Measurement Models

Finally, measurements are incorporated into our system to develop a realistic model of orbit determination uncertainty. We assume the usual radiometric measurements of Doppler data. As this is not a precision simulation, but a qualitative simulation, it is not necessary to model the Doppler data with high precision. Rather, we need a formulation that correctly incorporates the main contribution of these measurements into the orbit information matrix.

To incorporate the Doppler data measurement, we revisit the classic analysis of the information content from a single pass of Doppler data performed by Hamilton and Melbourne.[2] That analysis showed that the main information extracted from a Doppler pass is the location of the spacecraft in the plane-of-sky and the line-of-sight velocity of the spacecraft with respect to the Earth. If the orbit uncertainty dynamics are properly mapped between measurement passes and the basic measurement information incorporated into the SRIF matrix at each pass, we can realistically model the evolution of orbit uncertainty over time.

To first order the Doppler signal from a spacecraft is only a function of its radial speed (relative to the station), its declination above the Earth's equator, and its right ascension as measured relative to the tracking station. If we denote these three variables as a vector $Y = [\dot{r}, \delta, \alpha]$, where $\dot{r}$ is the radial rate, δ the spacecraft declination, and α its right ascension, and if we designate the Doppler measurement by $\dot{\rho}$, then the information content of a single tracking pass can be formulated as[16]

$$\Delta\Lambda = \frac{1}{\sigma_{\dot{\rho}}^2 T}\int_{-T/2}^{T/2}\left(\frac{\partial\dot{\rho}}{\partial Y}\right)^T\left(\frac{\partial\dot{\rho}}{\partial Y}\right)\mathrm{d}t \tag{14}$$

where T is the total tracking pass length and $\sigma_{\dot{\rho}}$ is the noise of the Doppler measurement. Carrying out the operations and integration yields

$$\Delta\Lambda = \frac{1}{\omega\sigma_{\dot{\rho}}^2\Delta t} \times \begin{bmatrix} 2\psi & 0 & -2B\sin\psi \\ 0 & (A^2/2)[2\psi - \sin(2\psi)] & 0 \\ -2B\sin\psi & 0 & (B^2/2)[2\psi + \sin(2\psi)] \end{bmatrix} \tag{15}$$

$$A = R_s\omega\sin\delta \tag{16}$$

$$B = R_s\omega\cos\delta \tag{17}$$

where R_s is the tracking station distance from the Earth's spin axis, δ is the spacecraft declination in the Earth frame, ω is the Earth's rotation rate, ψ is the half-angle of the tracking pass, $\sigma_{\dot{\rho}}$ is the Doppler measurement noise, and Δt is the time interval over which the noise value is defined. Usually, for X-band up/X-band down Doppler tracking data $\sigma_{\dot{\rho}} \sim 0.1$ mm/s for $\Delta t = 60$ s.

For a SRIF filter the inclusion of measurements is usually performed using Householder transformations[13] to update the SRIF matrix with the measurement partials, properly scaled to represent the data noise. Generally, Doppler measurements are scalar measurements, and the measurement partial is a simple row vector. However in our approach we combine the entire Doppler pass into one coupled measurement of the three quantities of range rate, declination and right ascension. Because these quantities are integrated over a pass of Doppler data, there is not a convenient description of them outside of the information matrix. To incorporate these measurements into the SRIF matrix, the measurement partial of these quantities must be computed, which in this case will be a matrix that the Householder transformation can accomodate.

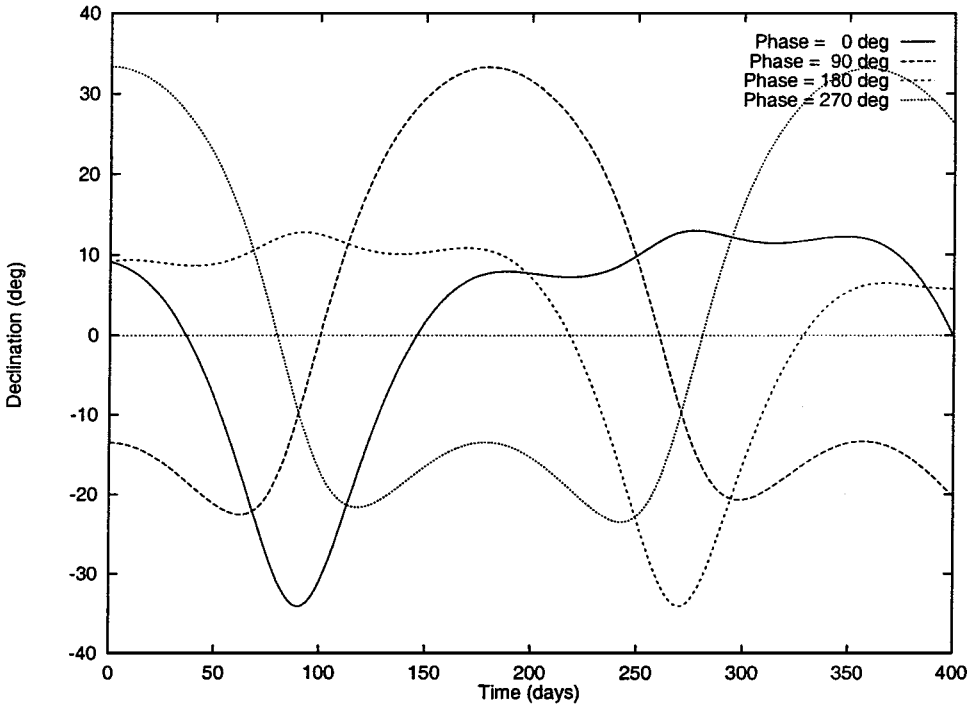

Fig. 6 Spacecraft declination angles for different initial phase angles. A 0-deg phase at epoch corresponds to the fall equinox, a 90-deg phase to the winter solstice, a 180-deg phase to the spring equinox, and a 270-deg phase to the summer solstice.

To derive this effective measurement partial, we note that the information matrix of a single Doppler pass can, itself, be expressed as a square-root matrix:

$$\Delta\Lambda = (\Delta R)^T \Delta R \tag{18}$$

Applying a square-root algorithm to the 3×3 matrix yields

$$\Delta R = \frac{1}{\sqrt{\omega\sigma_\rho^2 \Delta t}} \times \begin{bmatrix} \sqrt{2\psi} & 0 & \dfrac{-2B\sin\psi}{\sqrt{2\psi}} \\ 0 & \dfrac{A}{\sqrt{2}}\sqrt{2\psi - \sin(2\psi)} & 0 \\ 0 & 0 & B\sqrt{\psi + \sin(2\psi)/2 - 2\sin^2(\psi)/\psi} \end{bmatrix} \tag{19}$$

The general procedure for updating the spacecraft SRIF matrix given our measurement partial ΔR is to choose a Householder transformation T_H such that[13]

$$T_H \begin{bmatrix} R \\ \Delta R \end{bmatrix} = \begin{bmatrix} R' \\ 0 \end{bmatrix} \tag{20}$$

where R' is the new, updated SRIF matrix, which is then propagated forward in time.

With the current assumptions the information content of an entire Doppler measurement pass can be combined with the a priori information using purely analytical models. The use of such a simple model provides flexibility in simulating the effect of different tracking schedules and geometries, while not requiring that a detailed tracking schedule be implemented. To properly model the information content of the Doppler data, a transformation from the Earth equatorial coordinate frame to the Earth ecliptic frame (which is the frame that the spacecraft orbit is specified in) must be provided as well. This transformation introduces an additional free parameter into our analysis, which we formulate as a phase angle, but which really corresponds to the solar day at the start of the simulation. By varying this phase angle we vary the declination of the spacecraft over the time period in question. In general this will also cause the results of our orbit determination (OD) simulation to vary. Figure 6 shows declination histories of the trajectory depending on the initial phase angle.

E. Validation of the Model

To validate our simplified model of orbit determination mapping and uncertainty, a comparison of the overall results of our model were made with precision orbit determination studies performed for the Discovery mission Genesis.[17] Comparisons between our simplified model and the precision models at the Jet Propulsion Laboratory (JPL) yielded covariance agreements to an acceptable level, indicating that the simplified model captures the basic processes at work in this situation. Detailed comparisons between the results does not make sense because the Genesis study was made using high precision force and measurement models and a nonrepeating trajectory. The model used in this analysis has been carefully formulated to minimize inputs while retaining a realistic model of the orbit determination function. This design allows the model to be used for basic research into spacecraft navigation and orbit determination without having to specify detailed parameters. Also, the simple design allows for the entire model to be contained within a single program, eliminating the need for file transfers between the different functions of the model.

III. Theoretical Discussion

Having defined the unstable orbital system and the measurement and filtering approach, we can consider some basic theoretical predictions of how the spacecraft uncertainty will act as a function of time, measurement schedule, and stochastic acceleration.

A. Comparison with Traditional Approaches

The current situation differs strongly from traditional orbit determination analyses[3] in that the spacecraft's orbit is unstable. The usual situation found for planetary or solar orbits is that the spacecraft trajectory is a near-Keplerian elliptic orbit, and the uncertainty distributions are subject to, at worst, a polynomial instability associated with the energy integral of the two-body system. The familiar results from these systems is that the orbit uncertainty distribution grows along the "downtrack" direction of the nominal orbit, that is, along the direction of the local velocity vector. When mapped over

long time spans, this distribution deviates from a simple ellipsoid and becomes curved—just as the orbit itself is curved.[3] This case is of considerable interest, as it applies to the uncertainty distribution of most satellites and spacecraft, but it does not apply to the situation encountered in an unstable orbit, as defined here.

A variant on the uncertainty mapping of a simple conic orbit is found when one considers the effect of a planetary gravity assist (or a planetary moon gravity assist for spacecraft such as Galileo at Jupiter and Cassini at Saturn). In this situation an initial orbit uncertainty distribution is mapped through a hyperbolic orbit about the flyby body causing, in general, an expansion of the orbit uncertainty distribution after which increased tracking is usually called for to reestablish the quality of the orbit determination. For a satellite tour of a spacecraft about Jupiter or Saturn, where there may be several of these flybys in succession, the degradation of the original orbit uncertainty will grow considerably if a concerted effort at orbit redetermination is not carried out.

This last situation begins to mimic the situation that occurs when a spacecraft is flying in an orbit which is unstable. In this case the orbit uncertainty is continuously subject to a hyperbolic expansion and, in the absence of tracking, soon becomes twisted into a nonellipsoidal distribution. In this analysis we will only focus on the linear distribution of orbit uncertainty because in practical space flight the orbit uncertainty distribution is generally not allowed to become significantly nonellipsoidal.

B. Conservation of Phase-Space Uncertainty Volume

An interesting result from Hamiltonian dynamical systems is that the "volume" of phase space in a nondissipative dynamical system is conserved. This result also applies to the distribution of orbit uncertainty, meaning that the total volume of phase-space uncertainty (which is proportional to the square root of the determinant of the spacecraft covariance matrix) does not change over time under dynamical mapping. It is important to note that this applies to all Hamiltonian dynamical system, whether or not that system is time varying (such as a planetary satellite tour).[18] This result is easily seen from the linear mapping of the covariance matrix in time (with no stochastic dynamic parameters):

$$P(t, t_0) = \Phi(t, t_0) P_{t_0} \Phi^T(t, t_0)$$

combined with Liouville's Theorem, which implies that $|\Phi(t, t_0)| = 1$, where $|-|$ denotes the determinant function. Thus, were the spacecraft allowed to fly through its unstable trajectory without any orbit determination measurements the total volume of phase space in which the spacecraft can be found would be unchanged from its initial value, but the distribution of that phase-space volume would be markedly different and, in general, spread over a wide region of space.

The implication of this result in linear dynamics is that the orbit uncertainty becomes stretched out along the unstable manifolds of the local orbit, collapses along the stable manifolds of the local orbit, and becomes twisted onto itself in the central manifold. This picture is also extendable to the nonlinear orbit case, but now the orbit uncertainty distribution will become stretched into nonellipsoidal distributions—the only constraints being that the distribution must always remain connected and cannot self-intersect (derived from the uniqueness of solutions to the equations of motion).[19]

C. Effect of Stochastic Accelerations

The preceding picture is quite interesting, but it does not come to full fruition in the practical world of spacecraft analysis. In practice dynamical models of a spacecraft must incorporate the effect of small, unmodeled accelerations that act on the spacecraft. Although the effect of these small accelerations (measurable to less than 1 nm/s^2 with current orbit determination capabilities) is often negligible on the trajectory dynamics of the spacecraft, they exert a large effect on the dynamics of the orbit uncertainty.

These accelerations can be modeled as stochastic accelerations with a characteristic correlation time τ and a corresponding steady-state uncertainty level σ_a. It is instructive to integrate analytically the Ricatti equation for the orbit uncertainty of a one-dimensional force-free motion incorporating a stochastic acceleration with correlation time τ. The states in this system will be the position r, velocity v, and acceleration a of the body in question, and evaluation of the Ricatti equations will yield the equations:

$$\dot{\sigma}_{aa} = -(2/\tau)\sigma_{aa} + \sigma_\omega^2 \tag{21}$$

$$\dot{\sigma}_{va} = -(1/\tau)\sigma_{va} + \sigma_{aa} \tag{22}$$

$$\dot{\sigma}_{ra} = -(1/\tau)\sigma_{ra} + \sigma_{va} \tag{23}$$

$$\dot{\sigma}_{vv} = 2\sigma_{va} \tag{24}$$

$$\dot{\sigma}_{rv} = \sigma_{vv} + \sigma_{ra} \tag{25}$$

$$\dot{\sigma}_{rr} = 2\sigma_{rv} \tag{26}$$

where σ_ω^2 is the constant stochastic uncertainty acting on the acceleration (units of km^2/s^5). To simplify the discussion, we assume that the uncertainties are initially uncorrelated, or $\sigma_{va_0} = \sigma_{ra_0} = \sigma_{rv_0} = 0$. The analytical solution for the uncertainties then becomes

$$\sigma_{aa} = \sigma_{aa_0} e^{-2t/\tau} + \tfrac{1}{2}\tau\sigma_\omega^2(1 - e^{-2t/\tau}) \tag{27}$$

$$\sigma_{va} = \tau\sigma_{aa_0}(e^{-t/\tau} - e^{-2t/\tau}) + \tfrac{1}{2}\tau^2\sigma_\omega^2(1 - 2e^{-t/\tau} + e^{-2t/\tau}) \tag{28}$$

$$\sigma_{ra} = \tau\sigma_{aa_0}[(t - \tau)e^{-t/\tau} + \tau e^{-2t/\tau}] + \tfrac{1}{2}\tau^2\sigma_\omega^2(\tau - 2te^{-t/\tau} - \tau e^{-2t/\tau}) \tag{29}$$

$$\sigma_{vv} = \sigma_{vv_0} + \tau^2\sigma_\omega^2\left[t - 2\tau(1 - e^{-t/\tau}) + \tfrac{1}{2}\tau(1 - e^{-2t/\tau})\right] \tag{30}$$

$$\sigma_{rv} = \sigma_{vv_0} t + \tfrac{1}{2}\tau^2\sigma_\omega^2[t^2 - 2\tau t(1 - e^{-t/\tau}) + 2\tau^2(1 - e^{-t/\tau}) - \tau^2(1 - e^{-2t/\tau})] \tag{31}$$

$$\sigma_{rr} = \sigma_{rr_0} + \sigma_{vv_0} t^2 + \tfrac{1}{3}\tau^2\sigma_\omega^2\left[t^3 - 3\tau t^2 - 3\tau^2 t + \tfrac{3}{2}\tau^3(1 - e^{-2t/\tau})\right] \tag{32}$$

To further simplify the incorporation of the stochastic acceleration into the model, we neglect the transient contributions and only model the steady-state contribution. Letting $t \gg \tau$ in the preceding results and retaining only the largest order terms in t yields the simplified relations:

$$\sigma_{aa} = \sigma_a^2 \sim \tfrac{1}{2}\tau\sigma_\omega^2 + \cdots \tag{33}$$

$$\sigma_{va} \sim \tau\sigma_a^2 + \cdots \tag{34}$$

$$\sigma_{ra} \sim \tau^2\sigma_a^2 + \cdots \tag{35}$$

$$\sigma_{vv} \sim 2t\tau\sigma_a^2 + \cdots \tag{36}$$

$$\sigma_{rv} \sim t^2\tau\sigma_a^2 + \cdots \tag{37}$$

$$\sigma_{rr} \sim \tfrac{2}{3}t^3\tau\sigma_a^2 + \cdots \tag{38}$$

where the stochastic acceleration term σ_ω^2 has been replaced with the steady-state acceleration uncertainty σ_a (units of km/s^2), which has a clearer physical interpretation.

If the stochastic acceleration is set to zero, it is simple to confirm that the total volume of phase-space uncertainty, $\sigma_{rr}\sigma_{vv} - \sigma_{rv}^2$, is conserved for arbitrary time t. When the stochastic accelerations are included, however, this volume grows with time, asymptotically approaching $1/3\tau^2\sigma_a^4 t^4$. Thus, the stochastic accelerations cause the phase volume of uncertainty to grow with time, destroying the Hamiltonian nature of the phase-space dynamics.

This increase in phase-space uncertainty tends to destroy the effect of the stable manifolds, as now all portions of the phase space will in general grow in uncertainty over time. Its effect on the unstable manifolds is not as obvious, however. Because the unstable manifolds have an exponential increase in time and the stochastic accelerations only cause a polynomial increase in time, we still expect the unstable manifolds to play a dominant role in the distribution of uncertainty.

D. Effect of Stable and Unstable Manifolds on the Information Matrix

Before proceeding it is helpful to shift our attention to an alternate form of the orbit uncertainty distribution—the information matrix. Technically, the information matrix is the inverse of the orbit covariance matrix and is the generator of the orbit uncertainty ellipsoid:

$$\Lambda = P^{-1} \tag{39}$$

$$\delta x \cdot \Lambda \cdot \delta x \leq \sigma^2 \tag{40}$$

where δx traces out the orbit uncertainty in the phase space about the nominal trajectory and σ is the standard deviation level (sigma level) of the uncertainty ellipsoid (i.e., a 1-σ or 3-σ ellipsoid).

Although the effect of the stable manifold is to decrease the uncertainty distribution and the effect of the unstable manifold is to increase the uncertainty distribution of the orbit for the covariance matrix, their roles are reversed when considering the information matrix. This can be clearly seen for the case of no dynamic stochastic parameters when the information matrix maps according to

$$\Lambda(t, t_0) = \Phi^T(t_0, t)\Lambda_{t_0}\Phi(t_0, t)$$

where we note that $\Phi(t_0, t) = \Phi^{-1}(t, t_0)$. Under mapping by the inverse of the STM, motion along the stable manifolds will expand in time and motion along the unstable manifolds will contract, reversing their properties for forward motion in time. Thus, the unstable manifold will "deplete" information along its manifold direction, causing the information matrix to contain less content along these lines. Conversely the stable manifold will "accrete" information along its manifold direction, causing the information matrix to accumulate information. In the ideal case with no stochastic accelerations, the orbit information along the stable manifold naturally becomes better determined, whereas the orbit information along the unstable manifold naturally becomes more poorly determined. When stochastic accelerations are added to the system, they uniformly decrease the amount of information contained in the information matrix. Note from Eq. (12) that the stochastic accelerations can never completely remove the information content contained in the information (or SRIF) matrix.

To counter both these effects, the depletion of information along the unstable manifolds and the uniform depletion of information caused by the stochastic accelerations, it is necessary to add information (i.e., measurements) into the system. For spacecraft the usual source of this information is Doppler tracking, although there are a variety of other measurements available. In terms of the information matrix, the additional information from a track of Doppler data $\Delta\Lambda$ simply adds to the preceding information:

$$\Lambda' = \Lambda + \Delta\Lambda \tag{41}$$

where Λ is the original information matrix for the spacecraft and Λ' is the new information matrix. Because the covariance matrix is positive semi-definite, so too is the information matrix—meaning that a measurement cannot decrease the overall amount of information available.

Now, in principle the effect of adding a given amount of information in a direction that is depleted in information (i.e., along an unstable manifold) will be more efficient than adding that same amount of information along a direction that is well determined (i.e., along a stable manifold). This principle is also realized in that, because of the increased sensitivity of the unstable manifold, a measurement along that direction will allow the state to be better determined than a similar measurement along a state without that level of sensitivity. Or, stated differently, because a small error along the unstable manifold becomes enhanced and more observable as a result of the hyperbolic expansion, a measurement along that manifold will allow the initial error to be more accurately measured.

This principle, if verified with numerical simulation, may be the basis for the determination of optimal tracking periods or conditions along an unstable orbit. A major question is how this principle, clear for the ideal Hamiltonian case, becomes modified once a realistic case is modeled and stochastic accelerations are included.

IV. Orbit Uncertainty Dynamics

Having defined our model problem of an unstable orbit and the accumulation and mapping of information along that orbit, we carry out a number of simple computations to better quantify and understand the influence of the unstable orbit on the orbit information and uncertainty distribution. All our numerical calculations presented assume an initial phase angle of 270 deg; the resulting declination history can be found in Fig. 6. The latitude of the Doppler tracking station is assumed to be 30 deg and the pass angle to be 30 deg.

In the discussions we will use the direction of the local unstable manifold and the direction of the maximum orbit uncertainty in order to establish our results. As defined in Sec. II, the local unstable manifold for our trajectory is computed from the state transition matrix and corresponds to the eigenvector of the largest eigenvalue with magnitude greater than one. From Figs. 4 and 5 it is clear that this largest eigenvalue is unambiguously defined for the orbit under consideration. The direction of maximum orbit uncertainty is defined using the orbit covariance matrix. At each time step we compute the eigenvalues and eigenvectors of the covariance matrix and find the maximum eigenvalue of the matrix. The direction of maximum uncertainty is then defined by the eigenvector associated with the maximum eigenvalue. The influence of the local unstable manifolds on the orbit uncertainty distribution can then be gauged by comparing the relative directions of the unstable manifold and the maximum uncertainty. In the following this comparison is made by taking the dot product of these two directions, where because the eigenvectors of these matrices are six-dimensional, the dot product is taken between two six-dimensional vectors. When this projection is close to or equal to one, the unstable manifold can be considered to be exerting a strong influence on the orbit uncertainty distribution. When the projection is close to or equal to zero, the unstable manifold can be considered to be well-determined, indicating that the sensitivity of trajectories along this direction is aiding in its determination. If the unstable manifold and the maximum uncertainty direction were uncorrelated with each other, the average projection of these directions would lie in the range of 0.4 to 0.6.

A. Overall OD Performance

Using our base trajectory, we computed the OD uncertainty of the spacecraft over two halo orbit periods. Doppler passes are included every 2 or 25 days, and the trajectories have a steady-state stochastic acceleration of 10^{-16}, 10^{-12}, or 10^{-10} km/s^2 with correlation times of approximately $\frac{1}{2}$ day. Presented in Figs. 7 and 8 are plots of the average position and velocity uncertainties as a function of time. The average was computed by taking the trace of the appropriate submatrix of the covariance, dividing by three, and taking the square root. This gives us an overall measure of the orbit quality. It also confirms the steady-state expectations of the system. We note that the order-of-magnitude differences in the uncertainties match the expected order-of-magnitude difference from Eqs. (36) and (38).

B. Mapping of OD Uncertainties Without Measurements

To show that the direction of largest uncertainty no longer lies in the downtrack direction, the maximum uncertainty direction and local unstable manifold were projected onto the downtrack direction of the orbit. Were the downtrack direction still the dominant direction, we would expect the maximum uncertainty direction to approach a projection value of one with the downtrack direction. The results of this computation are shown in Fig. 9. This figure corresponds to a mapping of an initial orbit uncertainty distribution with no measurement updates. What is clear from this figure is that the unstable manifold and the maximum uncertainty directions approach each other and that the maximum uncertainty direction does not align itself with the downtrack.

To show this more clearly, we plot the projection of the maximum uncertainty direction onto the local unstable manifold in Fig. 10. As the projection approaches a value of unity, this clearly indicates that the unstable manifold controls the direction of maximum orbit uncertainty. The implication of this is that the direction of largest uncertainty, after mapping for a sufficiently long time period, will not be directly related to the geometry of the orbit but is instead related to the geometry of the unstable manifold, which

is a combination of both position and velocity directions in phase space.

To bring this effect into sharper focus, we project the maximum orbit uncertainty direction onto the unstable manifold direction and compute the time for the two directions to become aligned with each other. In Table 1 the entrainment time for the two directions to come within 10 deg of each other is given as a function of the amount of tracking prior to data cutoff and level of stochastic acceleration. The average characteristic time of the orbit is ~24 days (computed from the periodic orbit's largest characteristic exponent), thus the orbit uncertainty will grow by an order of magnitude in ~66 days. This correlates well with the time it takes the orbit uncertainty to become entrained along the unstable manifold. We note some variation in

Table 1 Time for the maximum uncertainty direction and the local unstable manifold to align within 10 deg of each other in the absence of tracking (This time varies with amount of tracking prior to data cutoff and steady-state level of stochastic accelerations.)

Days of tracking before data cutoff, days	Time to align to within 10 deg Stochastic accelerations		
	10^{-16}, km/s^2	10^{-12}, km/s^2	10^{-10}, km/s^2
2	68	68	58
50	67	45	41
100	79	62	58
150	89	57	62

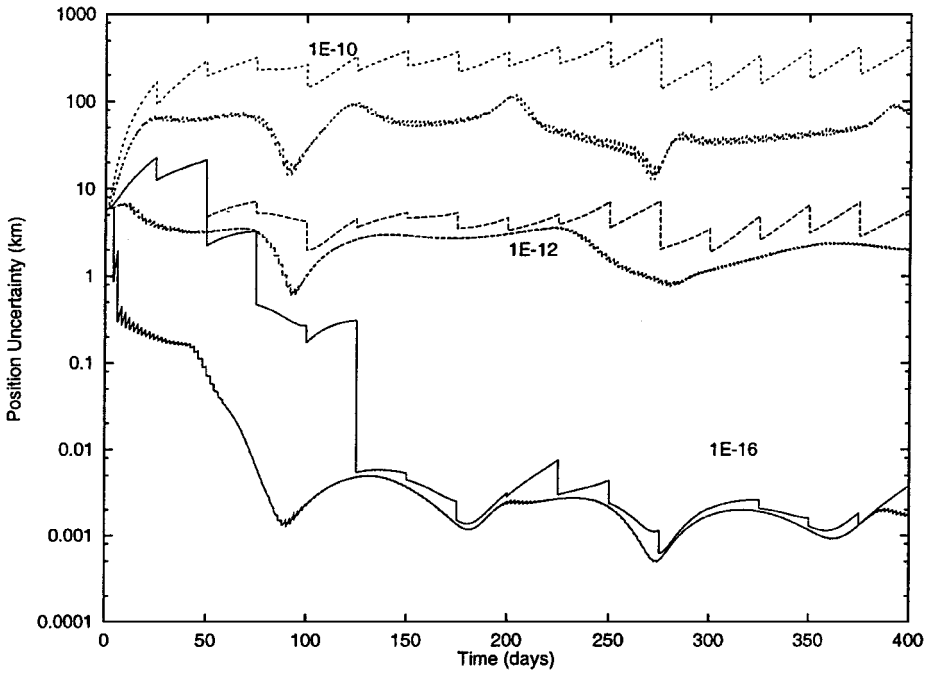

Fig. 7 Average position covariance for different stochastic acceleration levels and tracking schedules of every 2 days and every 25 days.

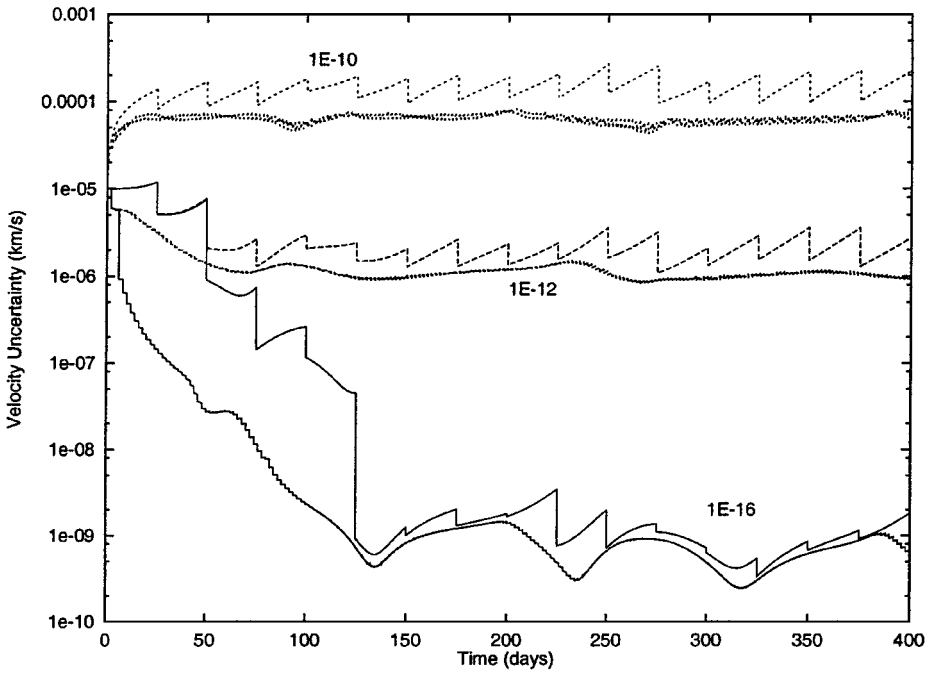

Fig. 8 Average velocity covariance for different stochastic acceleration levels and tracking schedules of every 2 days and every 25 days.

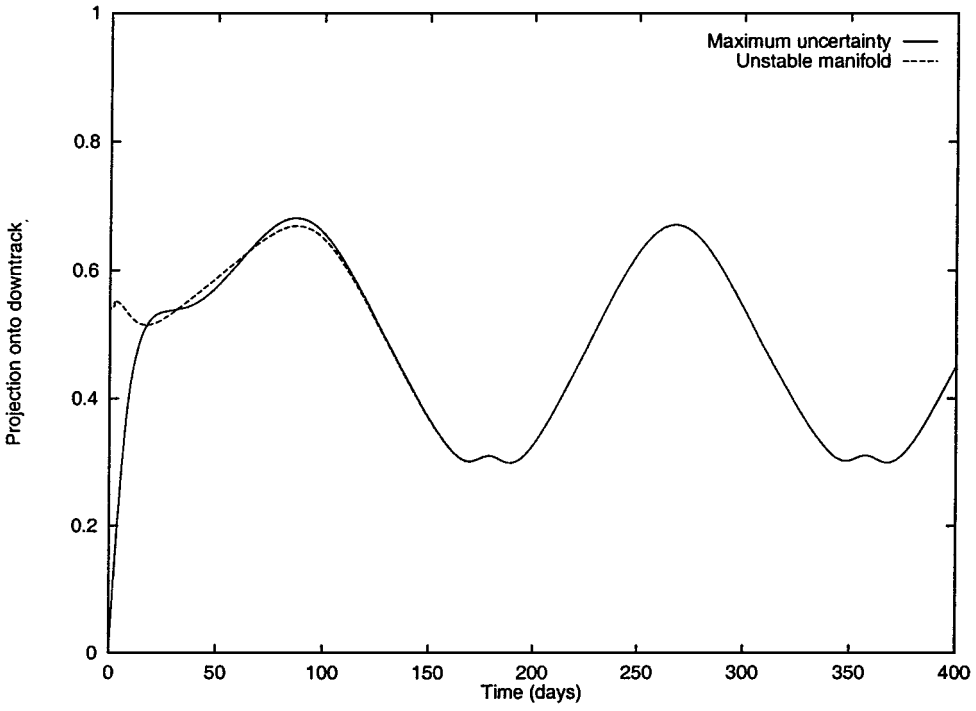

Fig. 9 Unstable manifold and maximum direction of uncertainty projected into the downtrack direction for a mapped uncertainty distribution with no measurements.

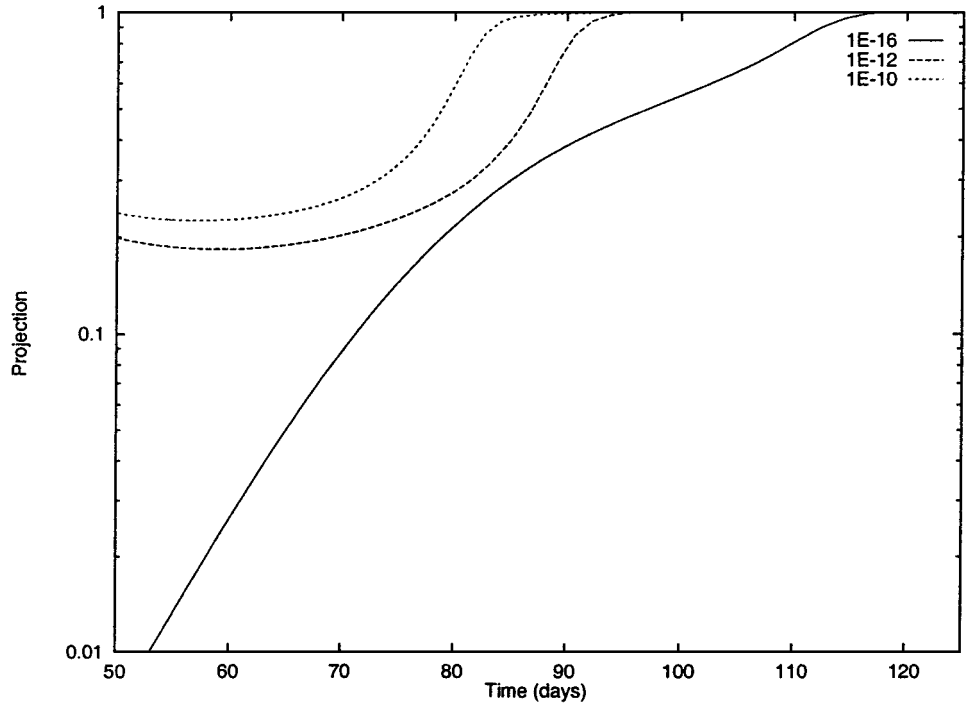

Fig. 10 Projection of the maximum direction of uncertainty along the unstable manifold. The projections are shown after 50 days of tracking with one pass every two days. Three different levels of stochastic acceleration are shown.

the entrainment time with the level of stochastic accelerations, with the clearest trend being a decrease in time for the larger values of stochastic acceleration. The variation across these parameters is not that significant, however, indicating that the unstable manifold continues to dominate the orbit distribution dynamics even when there are large stochastic accelerations present.

C. Effect of Measurements on OD Dynamics

Without measurements the STM directions and maximum covariance uncertainty directions approach each other asymptotically. With measurements this effect no longer holds, and the direction of maximum uncertainty and the unstable local manifold are no longer simply aligned. In Figs. 11–13 we show the projection of the maximum uncertainty direction onto the local unstable manifold, each figure corresponding to a different level of stochastic acceleration and each showing the distributions for a track every 2 and 25 days. Although complicated, there are some basic results that can be extracted from these plots. For the infrequent tracking schedule of one pass every 25 days there is an obvious trend for the maximum uncertainty direction to align with the unstable manifold, an effect that we characterized in the preceding section. Of specific interest, however, is that after the next measurement is incorporated the maximum

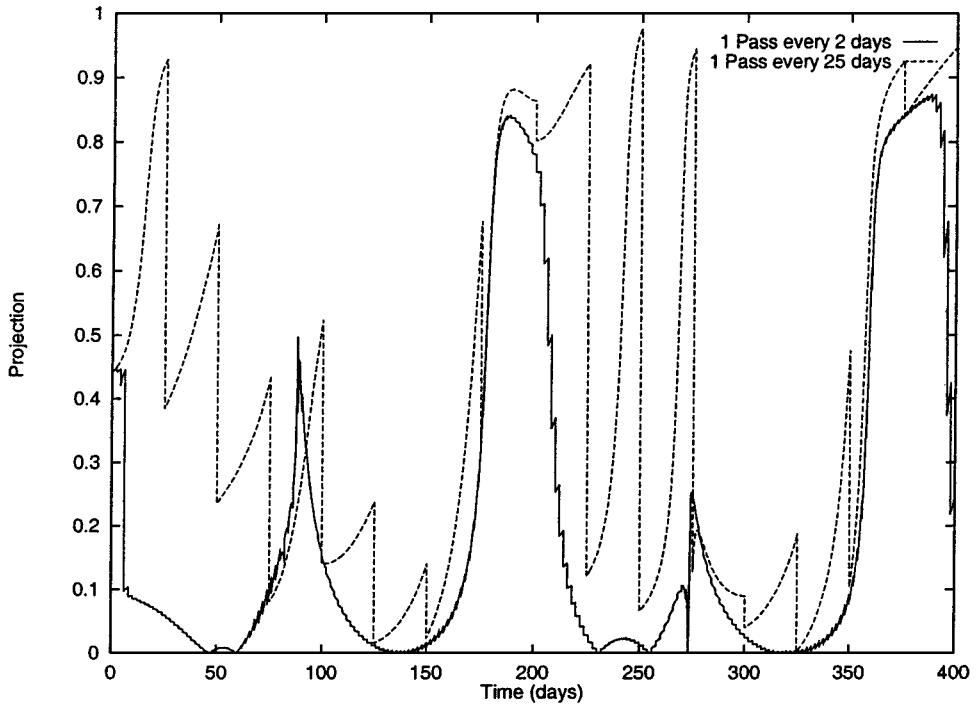

Fig. 11 Projection of maximum uncertainty direction onto the local unstable manifold for a track every 2 and 25 days with a stochastic acceleration level of 10^{-16} km/s^2.

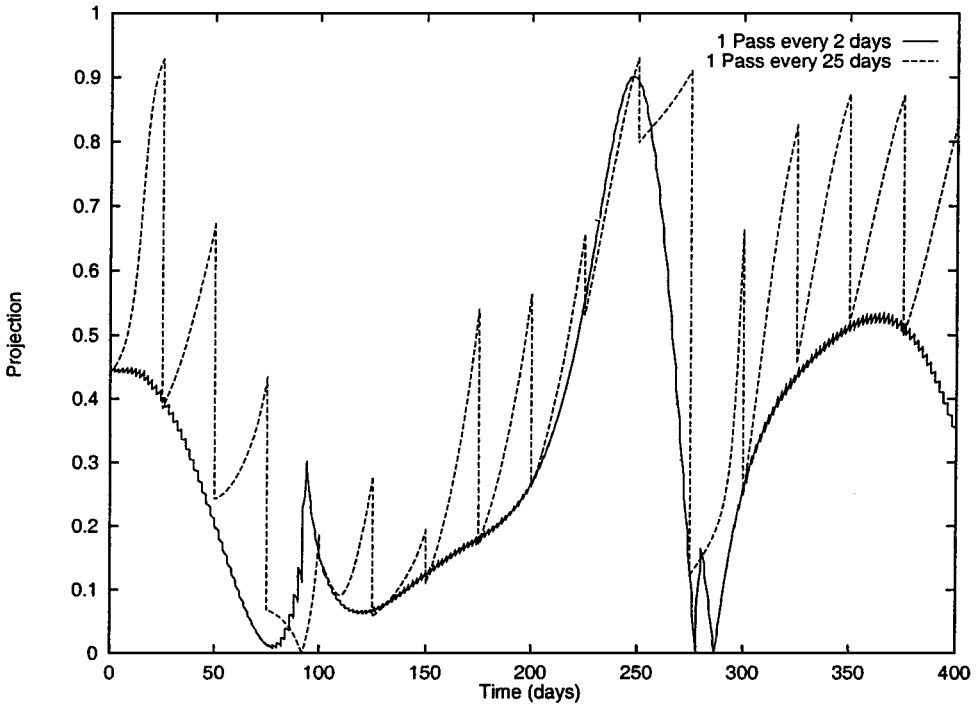

Fig. 12 Projection of maximum uncertainty direction onto the local unstable manifold for a track every 2 and 25 days with a stochastic acceleration level of 10^{-12} km/s^2.

uncertainty direction becomes more orthogonal to the local unstable manifold. This is direct evidence of the effect discussed earlier, which posited that, with tracking, the unstable manifolds should become better determined in general as a result of the increased efficiency of measurements along this direction. We see that this effect is pronounced for all levels of stochastic acceleration.

Next we note that the direction of maximum uncertainty tends to be orthogonal to the local unstable manifold, indicated in Figs. 11–13 by the projection being relatively small over most of the tracking history. Here, however, there are clear deviations from this effect, which should be explained. The same plots generated for different initial phase angles (or initial day of year) exhibit similar spikes in the alignment between the maximum uncertainty direction and the unstable orbit, although their distribution in time is different, indicating that the effect is caused by the relative geometry of the spacecraft and measurements. We also note a "smoothing" of the spikes with increasing level of stochastic acceleration. A comprehensive series of comparisons between this projection geometry and other dynamical quantities in the system show that the strongest correlation with these periods of alignment occur when the maximum direction of uncertainty is aligned along the direction which is "unsensed" by the Doppler measurements, in position space this

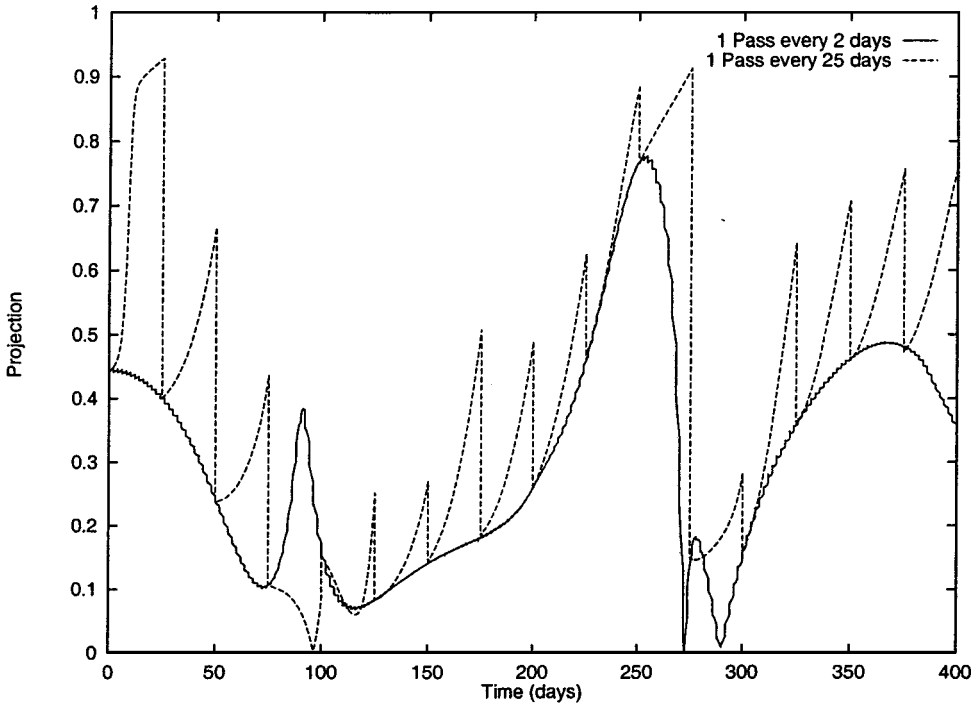

Fig. 13 Projection of maximum uncertainty direction onto the local unstable manifold for a track every 2 and 25 days with a stochastic acceleration level of 10^{-10} km/s^2.

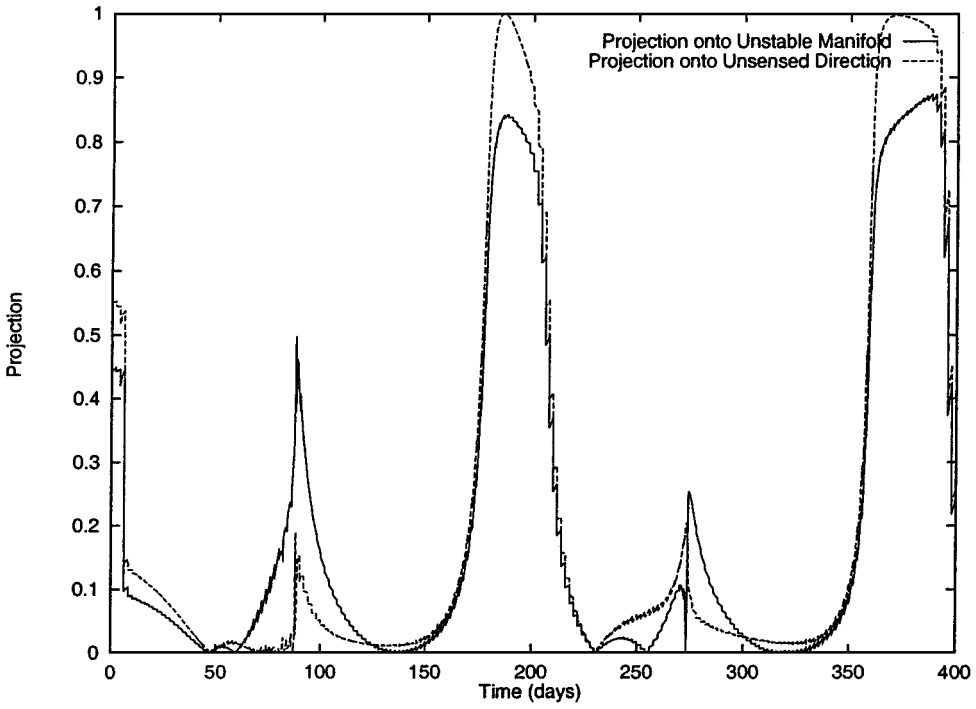

Fig. 14 Projection of maximum uncertainty direction onto the local unstable manifold and projection of maximum uncertainty direction into the unsensed direction for a Doppler pass, for the case of one pass every two days with a stochastic acceleration level of 10^{-16} km/s^2.

lies along the unit radius vector. Figures 14–16 overlay plots of the projection of the maximum uncertainty direction onto the local unstable manifold and into the unsensed direction of the Doppler measurements. The strong correlation between these two indicates that the effect of the increased sensitivity of the unstable manifolds is lost when it is not immediately detectable by the orbit determination measurements. The correlation in Figs. 14–16 is strongest for low levels of stochastic acceleration and becomes less strong for larger levels of stochastic acceleration. Periods when this alignment occurs appear to be most closely correlated with periods of slow or swift motion of the spacecraft across the celestial sphere. In either of these cases, apparently, the measurement conditions allow the unstable manifold to be unobservable for an interval of time.

The implications of these effects may be applicable to the design of simplified, robust navigation schemes for single or multiple spacecraft flying in unstable orbital environments. If a consistent prediction of the location and direction of the unstable manifolds can be found for a particular craft, it becomes possible to implement a sensing and control strategy that takes advantage of this effect. A detected growth of uncertainty along this direction could serve as an

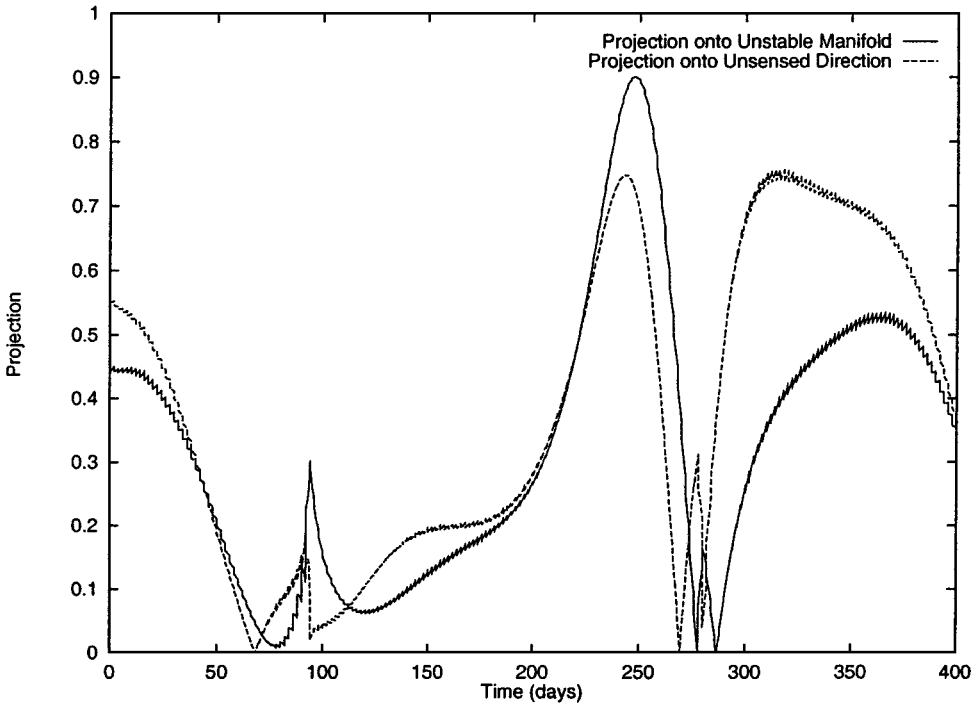

Fig. 15 Projection of maximum uncertainty direction onto the local unstable manifold and projection of maximum uncertainty direction into the unsensed direction for a Doppler pass, for the case of one pass every two days with a stochastic acceleration level of 10^{-12} km/s^2.

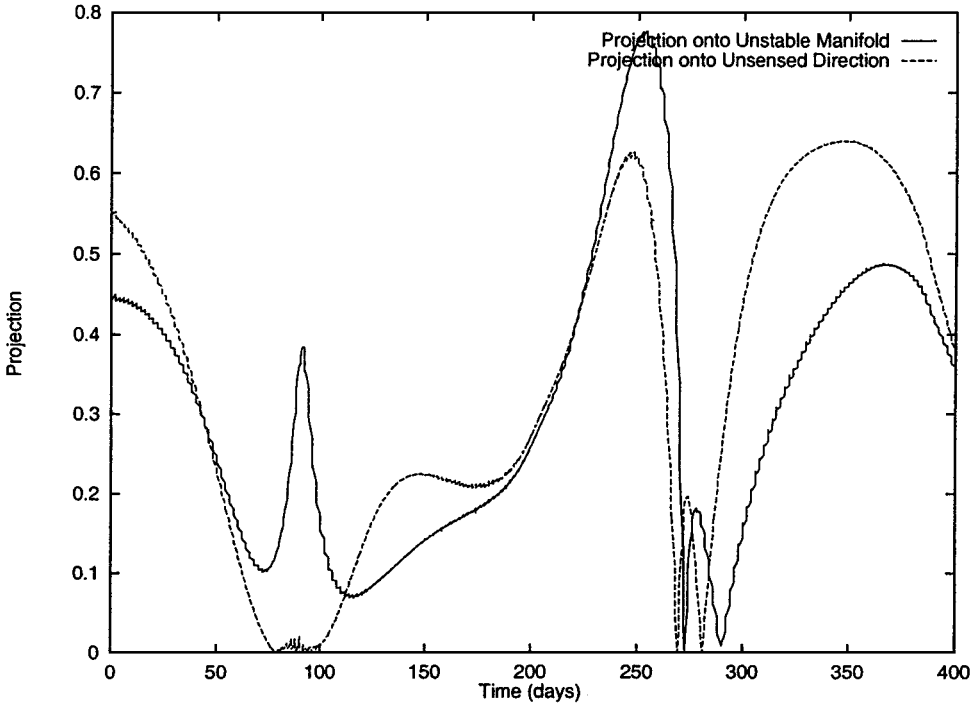

Fig. 16 Projection of maximum uncertainty direction onto the local unstable manifold and projection of maximum uncertainty direction into the unsensed direction for a Doppler pass, for the case of one pass every two days with a stochastic acceleration level of 10^{-10} km/s^2.

alert that the orbit determination or control scheme is not performing properly. Conversely, as a result of the increased efficiency of measurements along this direction, tracking schedules can be designed and optimized to take this into consideration.

V. Conclusions

This paper addresses, at a preliminary level, the linear dynamics of uncertainty distribution, with and without tracking, for a spacecraft in an unstable orbital environment (defined by the presence of positive finite time Lyapunov characteristic exponents). The numerical results model an orbital situation similar to the proposed Genesis halo orbit trajectory. Interesting results include the divergence of maximum uncertainty direction and the downtrack direction, the relation between the characteristic time of the instability and the time between tracking cessation and dominance of the unstable manifold over the orbit uncertainty distribution, the increased efficiency of measurements along the unstable manifold, and the tendency of the unstable manifold to be well determined during periods of tracking (when it is observable). These analyses were carried out using a square-root information matrix formulation for numerical robustness, using analytical models of Doppler tracking to account for measurements, and with correlated stochastic accelerations as an

input parameter. The models developed in this paper will be used in future studies of orbit determination in unstable orbital environments.

Acknowledgment

The research described in this paper was sponsored by the Telecommunications and Mission Operations Technology Program at the Jet Propulsion Laboratory, California Institute of Technology.

References

[1]Arnold, V. I., "Dynamical Systems III," *Encylopedia of Mathematical Sciences*, Vol. 3, Springer-Verlag, New York, 1988, pp. 72–75.

[2]Hamilton, T. W., and Melbourne, W. G., "Information Content of a Single Pass of Doppler Data from a Distant Spacecraft," *JPL Space Programs Summary*, Vol. 3, No. 37–39, 1966, pp. 18–23.

[3]Junkins, J. L., Akella, M. F., and Alfriend, K. T., "Non-Gaussian Error Propagation in Orbit Mechanics," *Journal of Astronautical Sciences*, Vol. 44, No. 4, 1996, pp. 541–563.

[4]Farquhar, R. W., "The Utilization of Halo Orbits in Advanced Lunar Operations," NASA TN D-6365, July 1971.

[5]Howell, K. C., Barden, B. T., and Lo, M. W., "Application of Dynamical Systems Theory to Trajectory Design for a Libration Point Mission," *Journal of Astronautical Sciences*, Vol. 45, No. 2, 1997, pp. 161–178.

[6]Scheeres, D. J., "The Restricted Hill Four-Body Problem with Applications to the Earth-Moon-Sun System," *Celestial Mechanics and Dynamical Astronomy*, Vol. 70, No. 2, 1998, pp. 75–98.

[7]Wintner, A., *The Analytical Foundations of Celestial Mechanics*, Princeton Univ. Press, Princeton, NJ, 1947, pp. 381, 382.

[8]Marchal, C., *The Three-Body Problem*, Elsevier, New York, 1990, pp. 146–158.

[9]Cesari, L., *Asymptotic Behavior and Stability Problems in Ordinary Differential Equations*, 2nd ed., Academic, New York, 1963, pp. 55–59.

[10]D'Azzo, J. D., and Houpis, C. H., *Linear Control System Analysis and Design*, 2nd ed., McGraw–Hill, New York, 1981, p. 615.

[11]Froeschlé, C., "The Lyapunov Characteristic Exponents—Applications to Celestial Mechanics," *Celestial Mechanics*, Vol. 34, No. 2, 1984, pp. 95–115.

[12]Scheeres, D. J., and Vinh, N. X., "Dynamics and Control of Relative Motion in an Unstable Orbit," AIAA Paper 2000-4135, Aug. 2000.

[13]Bierman, G. J., *Factorization Methods for Discrete Sequential Estimation*, Academic, New York, 1977, pp. 69–76.

[14]Battin, R. H., *An Introduction of the Mathematics and Methods of Astrodynamics*, AIAA Education Series, AIAA, New York, 1987, pp. 661–671.

[15]Scheeres, D. J., "Derivation of a Generalized Form of the SRIF Differential Equation," Jet Propulsion Lab., JPL Engineering Memo 314-564, Pasadena, CA, 1993 (internal document).

[16]Thurman, S. W., "Comparison of Earth-Based Radio Metric Data Strategies for Deep Space Navigation," AIAA Paper 90-2908-CP, 1990.

[17]Han, D., Carranza, E., Williams, B. G., and Scheeres, D. J., "Navigation Study Results for Genesis Mission," Jet Propulsion Lab., JPL IOM 312.A-97-016, Pasadena, CA, 15 July 1997 (internal document).

[18]Greenwood, D. T., *Classical Dynamics*, Dover, New York, 1997, pp. 182, 183.

[19]Nemytskii, V. V., and Stepanov, V. V., *Qualitative Theory of Differential Equations*, Dover, New York, 1989, pp. 3–38.